ORIGINAL PAPER

In situ formation of Co_3O_4 nanoparticles embedded N-doped porous carbon nanocomposite: a robust material for electrocatalytic detection of anticancer drug flutamide and supercapacitor application

Ramadhass Keerthika Devi[1] · Ganesan Muthusankar[2,3] · Shen-Ming Chen[1] [ORCID] · Gopu Gopalakrishnan[3]

Abstract

The one-step synthesis of heteroatom-doped porous carbons is reported with the in situ formation of cobalt oxide nanoparticles for dual electrochemical applications (i.e., electrochemical sensor and supercapacitor). A single molecular template of zeolitic imidazole framework-67 (ZIF-67) was utilized for the solid-state synthesis of cobalt oxide nanoparticle–decorated nitrogen-doped porous carbon (Co_3O_4@NPC) nanocomposite through a facile calcination treatment. For the first time, Co_3O_4@NPC nanocomposite derived from ZIF-67 has been applied as an electrode material for the efficient electrochemical detection of anticancer drug flutamide (FLU). The cyclic voltammetry studies were performed in the operating potential from 0.15 to -0.65 V (vs. Ag/AgCl). Interestingly, the fabricated drug sensor exhibited a very low reduction potential (-0.42 V) compared to other reported sensors. The fabricated sensor exhibited good analytical performance in terms of low detection limit (12 nM), wide linear range (0.5 to 400 μM), and appreciable recovery results ($\sim$98%, RSD 1.7% ($n = 3$)) in a human urine sample. Hereafter, we also examined the supercapacitor performance of the Co_3O_4@NPC-modified Ni foam in a 1M KOH electrolyte, and noticeable a specific capacitance of 525 F g^{-1} at 1.5 A g^{-1} was attained, with long-term cycling stability. The Co_3O_4@NPC nanocomposite supercapacitor experiments outperform the associated MOF-derived carbons and the Co_3O_4-based nanostructure-modified electrodes.

Keywords Metal-organic framework · ZIF-67 · Electrochemical sensor · Supercapacitor · Co_3O_4 · Flutamide · Anticancer drug

Introduction

Flutamide (FLU) is a specifically prescribed drug for prostate cancer treatment, which belongs to antiandrogen non-steroidal

✉ Shen-Ming Chen
smchen78@ms15.hinet.net

1 Department of Chemical Engineering and Biotechnology, College of Engineering, National Taipei University of Technology, No. 1, Section 3, Chung-Hsiao East Road, Taipei 106, Taiwan, Republic of China

2 Department of Mechanical Engineering, National Taipei University of Technology, Taipei, Taiwan

3 Department of Industrial Chemistry, Alagappa University, Karaikudi, Tamil Nadu 630003, India

medicines [1]. FLU prevents the metabolism of testosterone and thereby reduces the growth of prostate cancer cells [2]. Long-term exposure and excess concentration level of FLU in the human body caused adverse side effects, like rectal bleeding, liver malfunction, blood in urine, and uneven growth of male breasts [3]. After the oral consumption of FLU, it is excreted from the body via urine, usually in the form of 2-hydroxy flutamide and without the modified form of about 4.2%. And its consequences, FLU is transferred to the environment and becomes a threatening pollutant. Particularly in China, 13 different water sources were identified from FLU's contamination range of $\geqq$ 15 to 140 μg [4]. Thus, the detection of FLU in biological and environmental samples is a severe concern for effective cancer medication and environment quality control. Hence, advanced analytical techniques including positron emission tomography [5], high-performance

liquid chromatography [6], higher electrospray ionization mass spectrometry (ESI-MS) [7], and spectrophotometry [8] have been employed for the FLU detection. However, these techniques are suffered from high-cost instrumental setup, long operating time, and required more samples. In contrast, the electrochemical detection techniques are having advantages in terms of simple instrumental setup, low cost, rapid response, portability, high sensitivity, and selectivity [9, 10].

The selection of suitable electrode material plays a key role in electrochemical applications, viz., sensors and supercapacitors. Particularly, the electrode material with a porous structure can offer more reactive sites for interaction with the target analyte. Thereby, the sensitivity of the fabricated sensor will be enhanced. In this concern, incorporating metal oxide nanomaterials with conductive porous carbons can be the most effective strategy for the effective material design [11, 12]. Various protocols have been performed on the development and structural and morphological control of various metal oxide–decorated carbon nanomaterials for enhancing the electrochemical performances [13, 14]. Among them, cobalt oxide (Co_3O_4)–based nanomaterials have been receiving extensive research interest [15], owing to their good electrocatalytic nature, high theoretical capacitance, and environmental friendliness. Thus, it is expected that the integration of Co_3O_4 nanoparticles (Co_3O_4 NPs) with porous carbons will render outstanding performance. For that purpose, utilization of a self-sacrificial template as a solid precursor and its thermal conversion can be facile and effective strategy [16]. According to that, the choice of appropriate template is the significant factor for the materials synthesis. To construct such nanostructures, metal-organic frameworks (MOFs) are gifted materials and can be used as single molecular templates [17]. MOFs are made from organic ligands and metal-based nodes, exhibiting even and tunable pore sizes and distinct morphologies. The MOF derivatives can be a promising electrode active material due to the following characteristics: (1) the large surface area and high porosity facilitate the highly efficient mass transfer of the analytes/ions, and (2) the precise size and shape of the cavities provide good selectivity for specific molecules by the principle of size exclusion [18]. The beneficial features of high catalytic and ion storage capacity will help to construct efficient electrochemical sensors and supercapacitors.

Among the various MOFs, zeolitic imidazolate framework-67 (ZIF-67) is a fascinating material, which owns many active cobalt sites. ZIF-67 is isomorphous with zeolite and having a 3D framework, which is made up of Co(II) ions through 2-methylimidzloe (2mMI) linkers [19]. Thus, it can be transformed into Co_3O_4 NPs and/or nitrogen-doped porous carbon nanocomposite by the effect of direct one-step carbonization. Kuang et al. (2014) have demonstrated the synthesis of porous Co_3O_4 from ZIF-67 by optimizing the effect of calcination parameters [20], whereas Torad et al. (2014) have prepared the highly graphitized nanoporous carbon from ZIF-67, based on the calcination followed by acid etching treatment, and studied its supercapacitor performance [21]. Recently (2020), the same research group has developed the sensor for hazardous aromatic vapors by utilizing the ZIF-67-derived porous carbon [22]. However, ZIF-67-derived Co_3O_4 @ nitrogen-doped porous carbon for electrochemical sensing of flutamide (anticancer drug) is not yet reported to the best of our knowledge.

From the shed of light, herein, we have synthesized a simple solid-state transformation of ZIF-67 into the Co_3O_4 NP–loaded nitrogen-doped porous carbon (Co_3O_4@NPC) nanocomposite through calcination treatment, as shown in Scheme 1. So far, most of the reports focused on either sensor or supercapacitor applications. Here, we investigated the Co_3O_4@NPC nanocomposite–fabricated glassy carbon electrode (GCE) and Ni foam for the detection of FLU and supercapacitor performance, respectively. The unique structural features of the nanocomposite may influence the active sites on the surface and are expected to impact the electrochemical performances.

Experimental section

Materials and reagents

Cobalt nitrate hexahydrate ($Co(NO_3)_2.6H_2O$), 2-methyl imidazole ($C_4H_6N_2$, 2-mIM), flutamide ($C_{11}H_{11}F_3N_2O_3$, FLU), iso-propanol (C_3H_8O), ethanol (C_2H_5OH), N-methyl-2-pyrrolidone (C_5H_9NO, NMP), carbon black, and polyvinylidene difluoride (PVDF) were purchased from the SRL chemicals, India. All the analytical grade reagents were used as a received condition, and no further purification was performed. A stock solution of FLU was prepared using ethanol and stored in cooling conditions. The 0.1M phosphate buffer solution (PB) was prepared using sodium dihydrogen phosphate (NaH_2PO_4) and disodium hydrogen phosphate (Na_2HPO_4), and their pH values were adjusted by either NaOH or HCl as per the requirement.

Characterization and electrochemical measurements

The crystallinity of the samples was identified using powder X-ray diffraction (PXRD) studies. The materials' surface morphology was imaged from the field emission-scanning electron microscope (FE-SEM) and high-resolution transmission electron microscope (TEM). An energy-dispersive X-ray (EDX) spectroscopic analysis was performed to confirm the elements present in the nanocomposite. Further, the structural features were examined using X-ray photoelectron spectroscopic (XPS) measurements and Raman spectroscopic techniques.
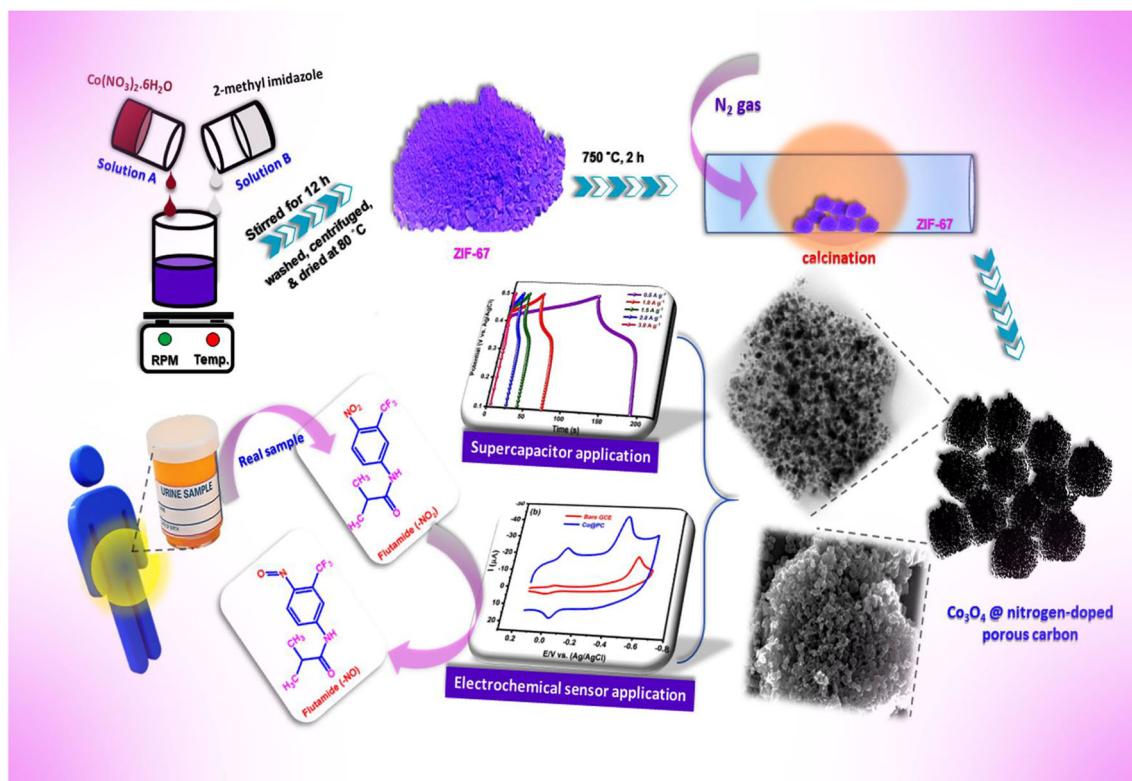
Scheme 1 Schematic illustration for the synthesis of Co_3O_4@NPC nanocomposite and its dual electrochemical application

Electrochemical studies were carried out using the CH Instrument (CHI-760C) electrochemical workstation. A conventional three-electrode system consisting of the glassy carbon electrode (GCE), saturated Ag/AgCl, and platinum wire served as a working electrode, reference electrode, and counter electrode, respectively. The modified electrodes' electrochemical behavior was analyzed using electrochemical impedance spectroscopy (EIS) and cyclic voltammetry (CV) techniques. The analysis was performed in a three-electrode electrochemical cell assembly, containing 5 mM of $[Fe(CN)_6]^{3-/4-}$ redox probe in 0.1 M KCl solution. The CVs were recorded in the potential from -0.4 to 0.8 V at the scan rate of 50 mV s^{-1}. The EIS data was documented in a frequency between 100 mHz and 100 kHz with a 10 mV amplitude. The analyte's electrochemical responses were examined using CV and differential pulse voltammetry (DPV) techniques in a phosphate buffer solution (PB; pH 7.0) at a scan rate of 50 mV s^{-1}. The FLU stock solution (10 mM) was prepared in ethanol and stored in a fridge when it was not used.

The supercapacitor studies were performed in a 1M KOH electrolyte solution containing a three-electrode system, where Co_3O_4@NPC nanocomposite–modified Ni foam substrate served as a working electrode and saturated Ag/AgCl and the platinum wire served as a reference and counter electrode, respectively. The specific capacitance value was calculated from the CV and the galvanostatic charge-discharge (GCD) measurements. In CV, $C_{spc} = Q/(m \times \Delta V)$, where

C_{spc} is specific capacitance (F g^{-1}), Q is average charge during CV scans, m is mass of the active material (g), and ΔV is working potential range (V). In the GCD method, $C_{spc} = (I \times \Delta t)/(m \times \Delta V)$, where I and Δt represent the current density (A) and discharge time (s), respectively.

Synthesis of ZIF-67

$Co(NO_3)_2 \cdot 6H_2O$ (0.4 g, 0.0137 M) and 2-mIM (5.0 g, 0.609 M) were separately dissolved in 100 mL of distilled water and stirred (500 rpm) well to get the homogenous solutions A and B, respectively. To solution A, the solution B was added dropwise. Upon addition, a purple color precipitate was obtained, which was further stirred (500 rpm) for 12 h in room temperature condition. The obtained purple-colored residue was recovered by centrifugation (5000 rpm) and washed thrice with deionized water and ethanol (100 mL each). Then, the product was dried at 80 °C overnight to get the ZIF-67 crystals.

Synthesis of cobalt oxide nanoparticles @ N-doped nanoporous carbon from ZIF-67

About 0.5 g of ZIF-67 was taken in a ceramic boat subjected to the heat treatment at 750 °C (heating rate 5 °C/min) for 2 h, with N$_2$ gas atmosphere, in a tubular furnace. After being heated, the sample was allowed to cool naturally. Then, the

resulted black color powder was known as Co_3O_4 NPs @ N–doped porous carbon (Co_3O_4@NPC) nanocomposite.

Fabrication of modified electrode

(i) Sensor

About 5 mg of Co_3O_4@NPC nanocomposite was dispersed in 1 mL of isopropanol and treated with ultrasonic waves in a bath sonicator to get the uniform dispersion. From the obtained black color suspension, a certain amount (1, 3, 5, 7, and 9 μL) was loaded on the polished GCE (3 mm) surface and dried at room temperature to get the Co_3O_4@NPC nanocomposite–modified GCE (Co_3O_4@NPC /GCE). Before the sensing studies, the Co_3O_4@NPC GCE was rinsed with DI water to eliminate the loosely attached particles.

(ii) Supercapacitor

For supercapacitor studies, Ni foam with an area of $\sim 1 \times 1$ cm^2 was utilized as a current collector. The slurry was prepared in N-methyl pyrrolidone solvent by mixing the Co_3O_4@NPC nanocomposite, carbon black, and PVDF in the ratio of 85:10:5. The slurry was then coated on the Ni foam by the doctor blade method and dried at 60 °C overnight. Prior to the experiment, the electrode was immersed in a 1M KOH electrolyte for few hours and utilized as a working electrode.

Results and discussion

Choice of materials

One-step in situ formation of metal oxide nanoparticles with hetero-atom-doped porous carbon nanocomposite possesses a tremendous advantage in material synthesis, in terms of simple preparation method, porous structure, high surface area, and high distribution of metal oxide nanoparticles in the carbon matrix. ZIF-67 is isomorphic with zeolite and has a 3D structure composed of Co(II) ions by 2-methylimidazole linkers. It can then be converted into Co_3O_4 NPs–loaded nitrogen-doped porous carbon (Co_3O_4@NPC) nanocomposite by direct one-step carbonization. Nanostructures of cobalt oxides are promising electrode material due to the fact of their electrochemical stability, high theoretical capacitance value, and high surface to volume ratio, which is more valuable for electrochemical sensors. Further, the nitrogen-doped carbon matrix offers high electrical conductivity, mechanical strength, and the supporting matrix for the metal oxide NPs. Considering these beneficial features, we have designed the Co_3O_4@NPC nanocomposite. And it is expected that the as-prepared nanocomposite can significantly enhance the

electrocatalytic performance in the FLU detection, in terms of very low detection limit, with high sensitivity, selectivity, and reproducibility.

Structural and morphology analysis

Purple-colored ZIF-67 MOF was obtained from the precipitation reaction between $Co(NO_3)_2 \cdot 6H_2O$ and 2-mIM using water at room temperature for 12 h. Afterward, a simple calcination treatment on ZIF-67 MOF produced the Co_3O_4@NPC nanocomposite, as displayed in Scheme 1. ZIF-67 owns a high porosity due to the zeolitic structure [23]. Interestingly, the Co^{2+} ions in ZIF-67 can be converted into a Co_3O_4 NPs; subsequently, it can catalyze the resulted carbons' graphitization during the carbonization of ZIF-67. The PXRD patterns of ZIF-67 and Co_3O_4@NPC nanocomposite are shown in Fig. 1a. The characteristic diffraction peaks of ZIF-67 are observed at 7.4°, 10.4°, 12.7°, 15.2°, 16.5°, 18.04°, 24.48°, and 26.7°, which corresponds to the (011), (002), (112), (022), (013), (222), (223), and (134) planes, respectively. The observed diffraction pattern confirms its arrangement as a zeolitic imidazole framework comprising of two mIM linkers per cobalt ($[Co(mIM)_2]$) in the unit cell [20]. After the calcination of ZIF-67 crystals, five new diffraction peaks at 31.2°, 36.88°, 44.7°, 59.4°, and 65.4° were observed and attributed to the (200), (311), (400), (511), and (440) planes, respectively. The observed pattern is well consistent with the standard data of Co_3O_4 (JCPDS #43-1003). No other peaks than Co_3O_4 were observed, suggesting the phase purity of the material. From the diffraction peaks of the Co_3O_4 NPs, the average crystallite size was calculated using the Debye-Scherrer equation [24], and it was found to be 26.33 nm.

Functional group analysis

The FT-IR spectra of ZIF-67 and Co_3O_4@NPC nanocomposite are given in Fig. S1, and they confirm the presence of various oxygen- and nitrogen-containing functional groups. The discussion about the FT-IR analysis on the materials is given in the supporting information. The Raman spectrum of Co_3O_4@NPC nanocomposite (Fig. S2) shows the five Raman active modes such as 1 E_g, 3 F_{2g}, and 1 A_{1g} at 472.8, (198.8, 516.3, 605.1), and 677.1 cm^{-1} respectively, which can be attributed to the values of pure Co_3O_4 spinel structure, further confirming the phase purity [25]. The Co_3O_4 with Co^{2+} and Co^{3+} states are positioned at tetrahedral (Td) and octahedral (Oh) sites, respectively. It is noted that the A_{1g} mode is more intense than other modes. It can be attributed to the characteristics of the Oh sites. The other modes, E_g and F_{2g}, are associated with the Td site's collective vibrations and Oh oxygen motions. Further, the Raman spectrum shows two major peaks of D (1348.7) and G (1594.5) bands due to the presence of carbon. The D band's intensity indicates the carbon lattice's
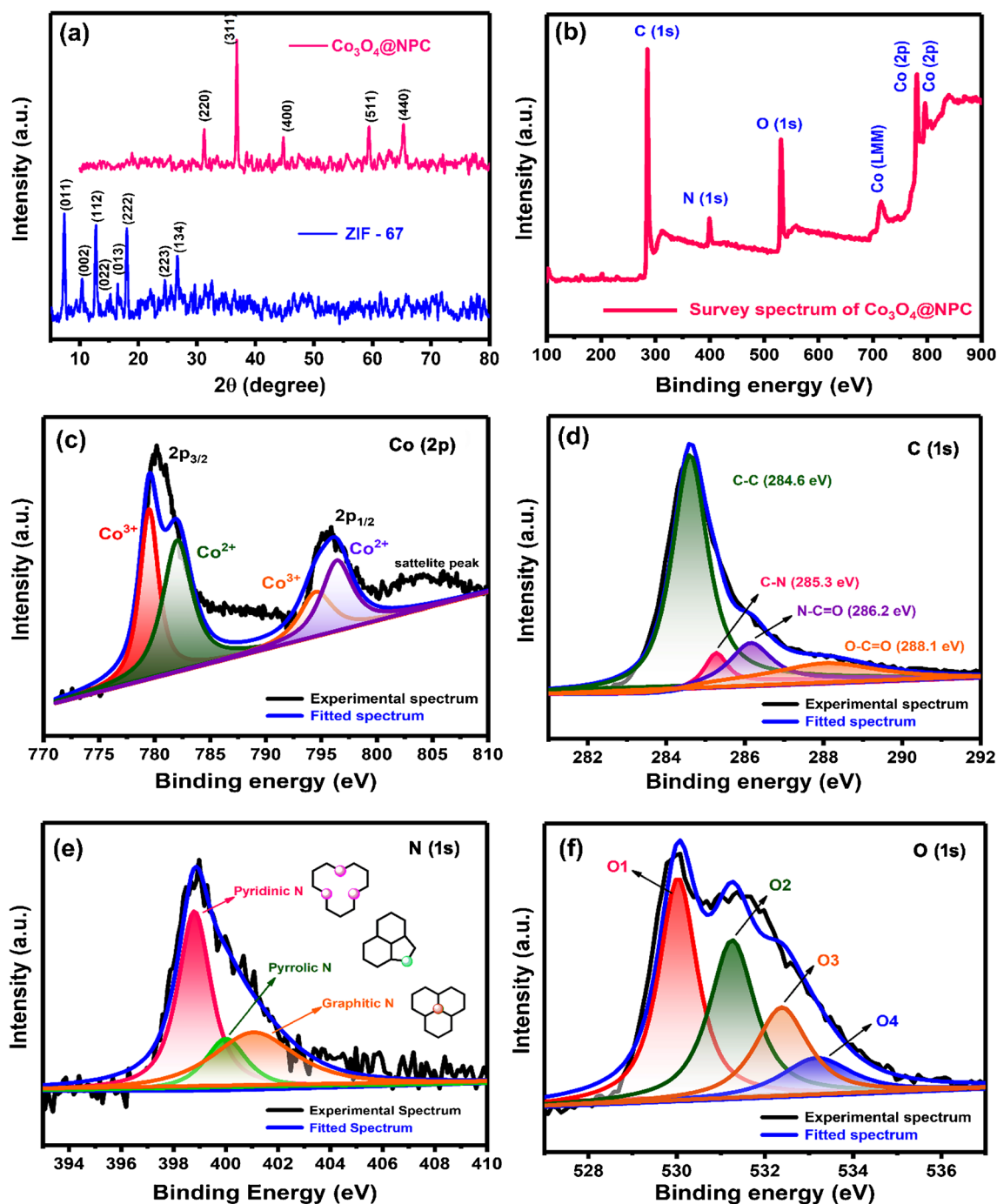
Fig. 1 **a** PXRD pattern of ZIF-67 and Co_3O_4@NPC nanocomposite. **b** XPS survey spectrum of the Co_3O_4@NPC nanocomposite, the deconvoluted spectrum of **c** Co 2p, **d** C 1s, **e** N 1s, and **f** O 1s

structural disorder due to the microstructure rearrangement and integration of N atoms into the lattice during the carbonization process. The G band is caused by the in-plane stretching vibration of graphitic sp^2-hybridized carbons [26], and they originated from the porous carbon present in the Co_3O_4@NPC nanocomposite. The intensity ratio between these bands (I_D/I_G) represents the degree of graphitization [27]. The I_D/I_G ratio of Co_3O_4@NPC nanocomposite is found

to be 1.06, confirming the presence of disordered graphitic carbon with a high surface area [28]. Also, the presence of Co_3O_4 NPs has acted as a catalyst to increase the degree of graphitization [15].

The oxidation states of the CO_3O_4 NPs and the composition of the nanocomposite were analyzed using XPS data as displayed in Fig. 1. The XPS survey spectrum (Fig. 1b) presents the prominent peaks of Co, C, N, and O. The core level

scan of Co (2p) reveals the two peaks positioned at 780.3 and 795.8 eV, attributed to the Co $(2p_{3/2})$ and Co $(2p_{1/2})$ spin states of Co_3O_4 NPs, respectively, which can be deconvoluted into various peaks of Co^{2+} and Co^{3+} as displayed in Fig. 1c, confirming the spinel structure of Co_3O_4. Moreover, the observed shakeup satellite peaks are due to the photoelectron emission between the Co atom's ground and excited states. The high-resolution spectrum of C 1s shows the major peak centered at 284.5 eV (Fig. 1d). The deconvolution yields four peaks at 284.6, 285.3, 286.2, and 288.1 eV, which corresponds to binding energies (BE) of carbon in a functional group such as sp^3 carbon, C-N, N-C=O, and O=C-O, respectively. Furthermore, N (1 s) peak at 398.8, 400.06, and 401.12 eV reveal the presence of pyridinic, pyrrolic, and graphitic nitrogen species, respectively (Fig. 1e). As a result, the nitrogen doping in the carbon matrix was confirmed. Besides, the deconvoluted peaks of O (1s) at the BEs of 530.03 (O1), 531.26 (O2), 532.26 (O3), and 533.17 (O4) eV can be C-OH (hydroxyl), C-O-C (epoxy), O=C-O (carbonyl), and carbonate structures, respectively (Fig. 1f). Overall, from the XPS analysis, a shift in binding energies of Co (2p) and O (1s), with reference to the reported values, reveals that the possibility of formation of Co_3O_4@NPC nanocomposite [29].

Surface morphology analysis

The surface morphology of the Co_3O_4@NPC nanocomposite was imaged from the FE-SEM analysis (Fig. 2a–c). It was observed that the nanosized particles of Co_3O_4@NPC nanocomposite were agglomerated and created microparticles with pores. However, these NPs were found to be in well homogeneousness throughout the mass. To get further insight into the morphology, HR-TEM analysis was performed (Fig. 2d–f). The results revealed that the Co_3O_4 NPs with diameters of 7 to 20 nm in size are evenly dispersed in the carbon matrix. The d-spacing value of the Co_3O_4 NPs is found to be 0.218 nm, which matches the (311) facet of Co_3O_4 NPs and in accordance with the XRD result. Further, the carbon surrounded the Co_3O_4 NPs, exhibiting the nanoporosity in its structure due to the effect of carbonization and the in situ catalysis of Co_3O_4 NPs [21]. The EDX analysis ((Fig. 2l) confirmed the presence of elements C (57.10%), N (10.01%), Co (6.77%), and O (26.22%) in the nanocomposite. Further, the atomic weight percentage (insight figure in Fig. 2l) of Co (6.77%) and O (26.22%) indicates the stoichiometric ratio of the Co_3O_4 NPs, which also confirms the successful formation of metal oxide and in good agreement with the XRD and Raman results. Further, the elemental mapping (Fig. 2g–k) of the Co_3O_4@NPC nanocomposite shows the homogenous distribution of the elements in the material.

Electrochemical characterization of modified electrodes

Electrochemical surface properties of the bare and modified electrodes were analyzed using the EIS and CV techniques in the redox probe of 0.1-M KCl solution containing 5 mM $[Fe(CN)_6]^{3-/4-}$ system. Electrochemical charge transfer resistance (R_{ct}) of bare GCE and Co_3O_4@NPC /GCE was measured by EIS analysis, and its results are shown in Fig. 3a, in the form of a Nyquist plot. The observed semicircles replicate the R_{ct} of the bare and modified electrodes. The inset figure in Fig. 3a shows the equivalent electrical circuit for the observed EIS data. From the results, the R_{ct} values are found to be 275 and 20 Ω for bare GCE and Co_3O_4@NPC/GCE, respectively. The low R_{ct} value of Co_3O_4@NPC/GCE indicates the fast electron transport is possible between the electrode/ electrolyte interface. Due to the synergistic effect between the Co_3O_4 NPs and well-graphitized NPC enhances the electrical conductivity. Thus, it revealed that the modified GCE could provide an easy electron transport pathway to the electroactive species.

The CVs of the bare GCE and Co_3O_4@NPC/GCE in the redox probe are displayed in Fig. 3b. Both electrodes exhibited the well-defined redox peak with the peak-to-peak separation ($\Delta E_p = E_{pa} - E_{pc}$) value of 130 and 90 mV, respectively. Comparatively, the bare GCE shows a high ΔE_p value, suggesting the low electrical conductivity. In contrast, the low ΔE_p value of Co_3O_4@NPC/GCE indicates better electron transport than bare GCE owing to the higher active surface area (A_{eff}). The observed CV results are well consistent with the EIS results. Further, to measure the A_{eff} of the Co_3O_4@NPC/GCE, a different scan rate study was performed in the redox prob. solution, and its CVs are shown in Fig. 3c. The increase in scan rate from 10 to 100 mV s^{-1} causes the redox peak current to increase linearly. And its linear relationship has been established between the square root of the scan rate and redox peak current, as shown in Fig. 3d. From the linear plot's slope value, the A_{eff} was calculated using the Randles-Sevcik Eq. (1).

$$I_p = \left(2.69 \times 10^5\right) n^{3/2} D^{1/2} v^{1/2} A C^* \tag{1}$$

where I_p, n, D, v, A, and C are the redox peak current, transferred number of electrons ($n = 1$), diffusion coefficient, scan rate, effective surface area, and concentration. The calculated A_{eff} of the Co_3O_4@NPC/GCE is 0.112 cm^2, whereas the bare GCE shows 0.078 cm^2. From the above results, it can be concluded that the Co_3O_4@NPC/GCE possesses an excellent electron transport pathway and high surface area than bare GCE. Thus, it is expected that the Co_3O_4@NPC/GCE can be an efficient electrode material sensor application.
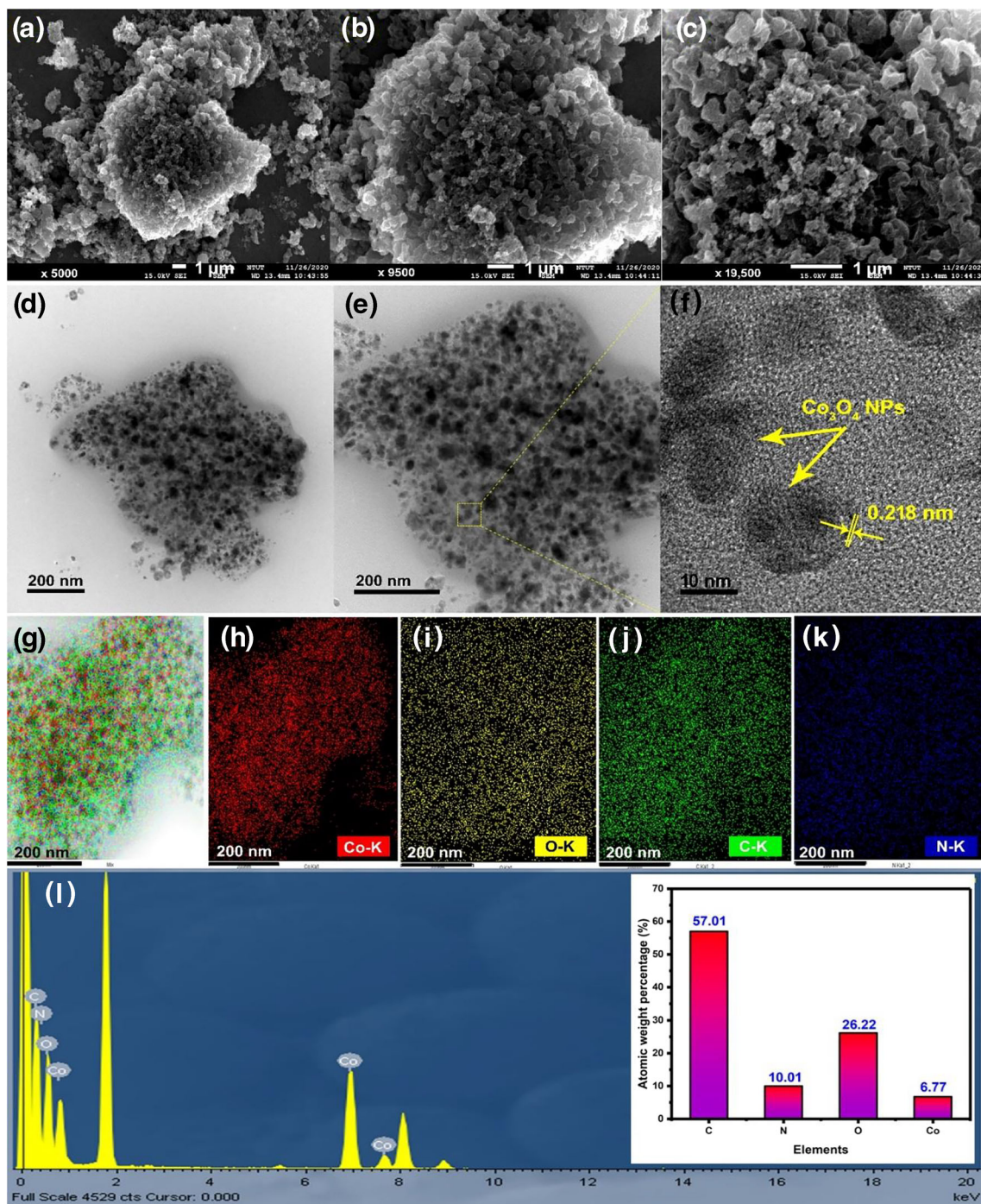
Fig. 2 FE-SEM images **a** 1 μm × 5000, **b** 1 μm × 9500, **c** 1 μm × 19,500 magnifications of Co_3O_4@NPC nanocomposite. HR-TEM images of Co_3O_4@NPC nanocomposite at **d**, **e** 200 n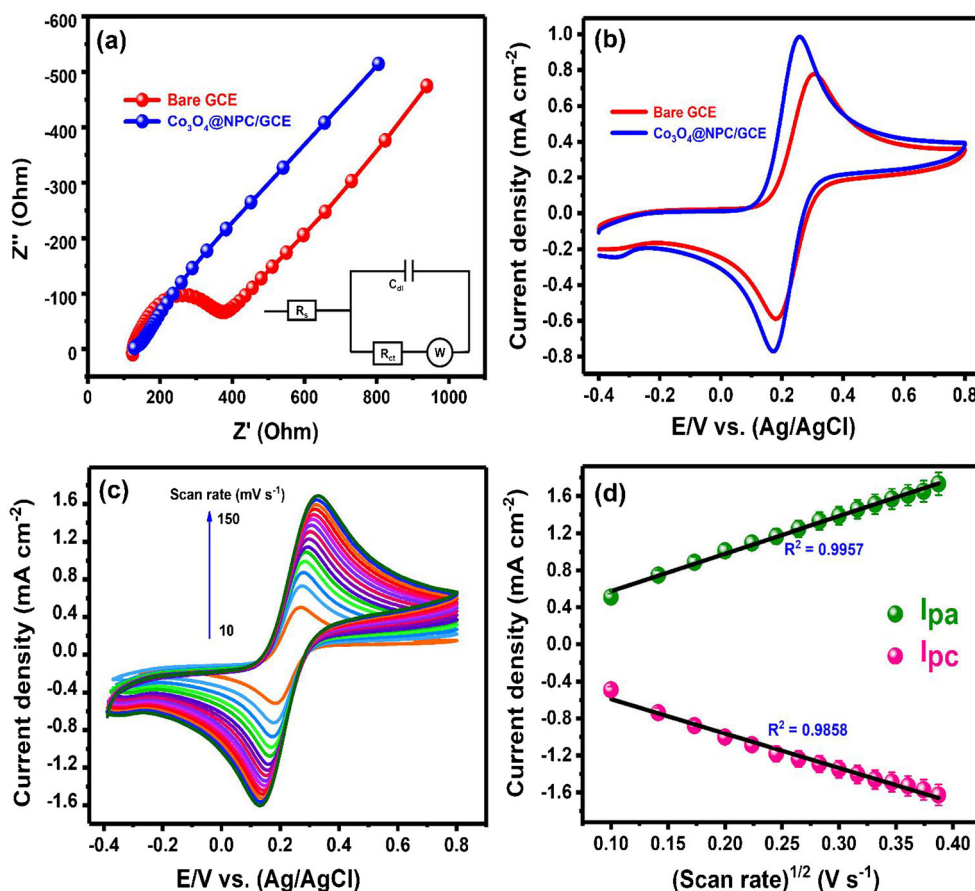m, **f** 10 nm magnifications. Element mapping results of **g** mixed elements, **h** Co, **i** O, **j** C, **k** N, and **l** the corresponding EDX spectrum of the nanocomposite (insight: atomic weight percentage of the elements)

Electrochemical performance of FLU on the electrode surface

The electrochemical response of FLU at bare GCE and Co_3O_4@NPC/GCE was studied using the CV technique. The experiment was performed between the potential window of + 0.15 and − 0.65 V in 0.5 M PB (pH 7.0) at the scan rate of 50 mV s^{-1}. Figure 4a shows the typical CV profiles of bare and Co_3O_4@NPC/GCE in the absence of FLU. It can be seen that the Co_3O_4@NPC/GCE has exhibited a tremendous enhancement of capacitive current when compared to the bare GCE. It might be due to the porous nature of the material and its high surface area. Besides, the CV profiles of the bare and Co_3O_4@NPC/GCE in the presence of 200 μM of FLU are

displayed in Fig. 4b. At bare GCE, a reduction peak (R1) of FLU was observed at − 0.55 V (E_{pc}) with the minimum cathodic peak current (I_{pc}) of − 0.26 mA cm^{-2}, and weak redox peak (O1&R2) were also detected. The results suggest the sluggish electron movement between the electrode surface and electrolyte. As a consequence, a high cathodic potential has been required for the reduction (R1) process.

By comparison, when the GCE was modified with Co$_3$O$_4$@NPC nanocomposite, an enormous increase in redox peak current was observed. However, to optimize the volume of nanocomposite loading, it varied between 1, 3, 5, 7, and 9 μL, and the respective CV results are shown in Fig. S3. It was noted that the redox peak current intensity was steadily increased from 1 to 3 μL and reached a maximum at 5 μL. Beyond that, the redox peak strength was significantly reduced, suggesting that the higher concentration of catalyst may hinder the electron transfer process to the active sites and interface between the electrode and analyte. At an optimized loading volume of 5 μL, the highest reduction peak current (I_{pc}) of − 0.57 mA cm^{-2} was achieved with a reduction potential of (E_{pc}) -0.42 V. Compared to the bare GCE, the nanocomposite-modified GCE reduces the FLU to a lower potential, indicating its good electrocatalytic efficiency.

Additionally, a well-marked redox peak, such as the oxidation peak (O1) at − 0.02 V and reduction peak (R2) at −

0.05 V, was also observed. The enhanced performance of Co$_3$O$_4$@NPC/GCE is due to the porous structure of the nanocomposite. A more significant number of electrolyte ions and FLU were accumulated at the pore sites and formed an electric double layer on its surface. As a result, the capacitive current increased and resulted in excellent electrocatalytic efficiency. In addition, the Co$_3$O$_4$@NPC/GCE displays nearly 25 times the lower peak (R1) current of the bare GCE. Therefore, the findings underscored the enhanced electrochemical efficiency of the Co$_3$O$_4$@NPC/GCE, which could be due to its superior electron conductivity, wide surface area, and short electron transfer pathway.

In a FLU detection process at the surface of Co$_3$O$_4$@NPC/ GCE, the observed cathodic peak (R1) is due to the irreversible reduction reaction of the nitro group (-NO$_2$) into a hydroxylamine (-NH$_2$OH) group, which involves the four-electron transfer mechanism (Fig. 5c). Further, the peaks O1 and R2 showed a quasi-reversible process during the first CV scan. Upon the second scan, distinct reversible peaks have resulted. The redox pair, O1 (E_{pa} = −0.02 V, I_{pa} = 0.22 mA cm^{-2}) and R2 (E_{pc} = −0.05 V, I_{pc} = −0.31 mA cm^{-2}) were due to the oxidation of hydroxylamine (-NH$_2$OH) into nitroso (-NO) group and the vice-versa (Fig. 5c). The resulting CV peaks and its consisting electrochemical reaction of FLU agree with the literature's reported mechanism [30, 31].

Fig. 4 CVs of bare GCE and Co$_3$O$_4$@NPC/GCE **a** without the presence of FLU and **b** in the presence of 200 μM FLU. **c** CVs of Co$_3$O$_4$@NPC/GCE at a varying scan rate (20 to 180 mV s^{-1}) in 200 μM of FLU in 0.1 M PB (pH 7.0) and **d** the linear plot of reduction peak current vs. scan rate
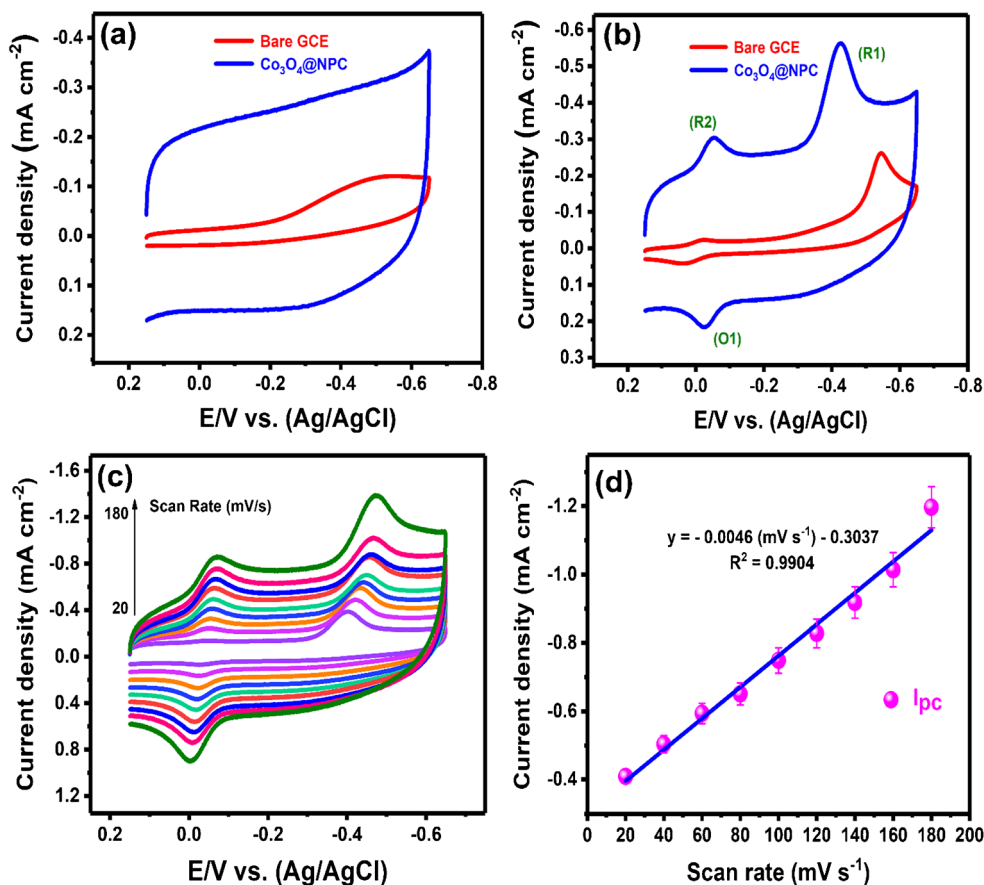
Effect of scan rate and pH

The scan rate effect for the detection of FLU at Co$_3$O$_4$@NPC/GCE was examined by varying the scan rates from 20 to 180 mV s^{-1} in the presence of 200 μM FLU in PB (pH 7.0). The observed CVs are displayed in Fig. 4c. Upon increasing the scan rate, the I$_{pc}$ was linearly increased with the slight shift of the E$_{pc}$ towards the negative potential side. A plot between the scan rate and I$_{pc}$ yield a good linear plot (Fig. 4d), and the corresponding linear regression equation is I$_{pc}$ (mA cm^{-2}) = −0.0046 (mV s^{-1}) − 0.3037 (R^2 = 0.9904). The result indicates that the electrocatalytic reaction of FLU at Co$_3$O$_4$@NPC/GCE is governed by an adsorption-controlled process [32]. The electrolyte's pH is a key parameter for the sensors, which influences the sensors' sensitivity. So, the effect of pH towards the FLU (150 μM) detection at Co$_3$O$_4$@NPC/GCE was investigated with different pH conditions (pH 3.0 to 11.0) of PB at the scan rate of 50 mV s^{-1}. The corresponding CV responses (Fig. 5a) depict that the increase in pH from 3.0 to 7.0 resulted in the increment of cathodic peak current. After that, it decreased at pH 9.0 and 11.0, and the reduction potential also shifted to the more negative potential side. Figure 5b shows the changes in reduction peak current intensity at different pH. Depending upon the electrolyte pH, the reduction potential was shifted to either a positive or negative direction.

It reveals that the electrochemical reaction of FLU at Co$_3$O$_4$@NPC/GCE is pH dependent. The observed trend revealed that a weak acidic or neutral condition is sufficient for the reduction reaction, implying that the FLU is a strong base. As a result, a weak acidic or neutral pH condition may offer the proper orientation for the effective electrocatalytic reduction of FLU. From the literature, it has been identified that around pH 6.0–8.0 is an optimum pH range for detecting flutamide [3, 30]. Moreover, the pH level of biological fluids and nitro compound polluted wastewater belongs to this pH range. Thus, we have chosen a pH of 7.0 as an optimum pH condition for further electrochemical investigations. The calibration plot between pH and E$_{pc}$ is shown in Fig. 5b, and its linear regression equation is E$_{pc}$ (V) = −0.0451 [pH] − 0.1149 (R^2 = 0.9902). The derived slope value (− 45 mV/pH) of the calibration plot is near to the theoretical Nernstian slope value (− 59 mV/pH), suggesting the contribution of an equivalent number of protons and electrons during the electrochemical reaction of the FLU at Co$_3$O$_4$@NPC/GCE.

Determination of FLU

The trace level determination of drugs, hazardous chemicals, and heavy metals is usually performed using the DPV technique because of its high sensitivity. Thus,
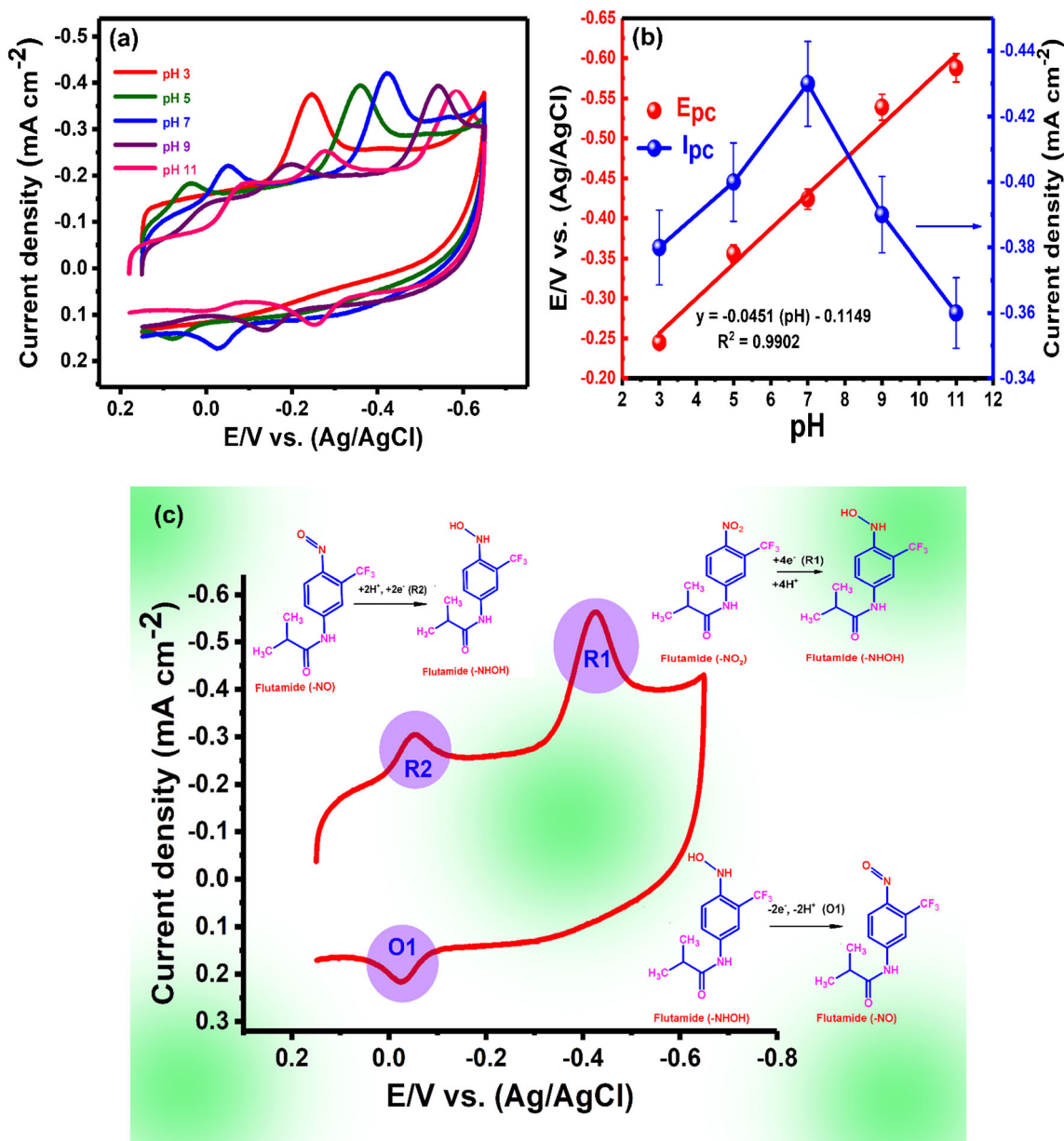
Fig. 5 **a** CVs of Co₃O₄@NPC/GCE at different pH from 3 to 11 (phosphate buffer) in the existence of 150 μM FLU **b** plot for pH vs.I$_{pa}$ (for R1), and calibration plot for pH vs. E$_{pa}$ (for R1), and **c** Possible electrochemical redox mechanism of FLU at Co₃O₄@NPC/GCE

the sensitive electrocatalytic determination of FLU at Co₃O₄@NPC/GCE was carried out using DPV protocol in PB at the scan rate of 50 mV s^{-1}. The experiment was performed between the potential of − 0.2 and − 0.6 V with the increasing concentration of FLU from 0.1 to 590 μM, and the obtained DPV signals are displayed in Fig. 6a. A sharp cathodic peak was observed at − 0.34 V and increased steadily as FLU concentration increased. A calibration plot (Fig. 6b) between the cathodic peak current and the concentration of FLU resulted in a linear plot with the linear regression equation of I$_{pc}$ (mA cm^{-2}) = −0.1930 C(μM) − 41.9538 (R^2 = 0.9976). The limit of detection (LOD) and sensitivity is determined from the

calibration plot's slope value using the equation of LOD = 3σ/S, where σ is the standard deviation of the blank response and S is the calibration plot's slope value.

From the calculation, the LOD of the developed sensor was found to be 12 nM. The analytical parameters like reduction potential, linear range, LOD, and sensitivity of the established sensor are compared to the previously reported sensing protocols, and it is presented in Table S1. The comparison table revealed that the Co₃O₄@NPC nanocomposite could reduce the FLU to the lowest reduction potential than other reported sensors. Thus, the developed sensor Co₃O₄@NPC/GCE may therefore be a promising candidate for the effective electrocatalytic detection of FLU.

Fig. 6 **a** DPVs of Co$_3$O$_4$@NPC/GCE at increasing concentration FLU (a to l = 0.1 to 590 μM) and **b** calibration plot for peak current vs. FLU concentration, **c** DPV responses of Co$_3$O$_4$@NPC/GCE for the reduction peak current of FLU (200 μM) with the co-existence of a 50-fold excess concentration of various nitro compounds, and **d** the corresponding relative error percentage bar diagram of interference study
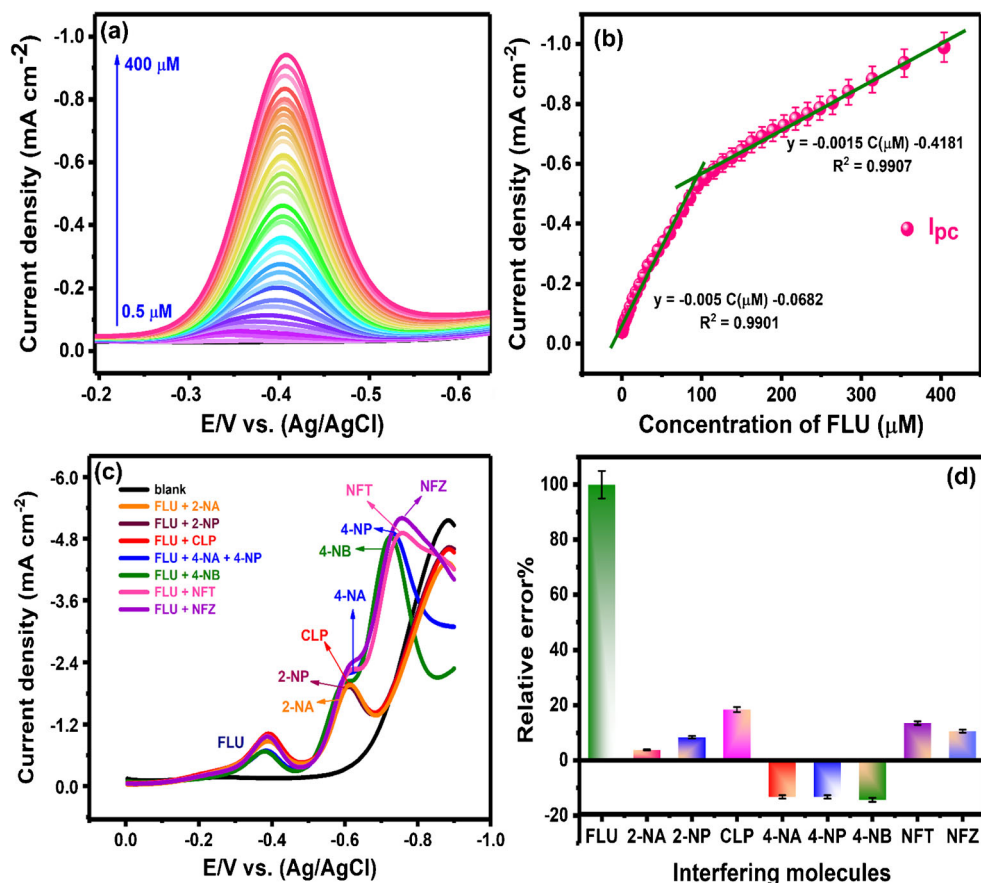
Interference, storage stability, repeatability, and reproducibility studies

The Co$_3$O$_4$@NPC/GCE's practical applicability was investigated based on repeatability, reproducibility, and selectivity studies using the DPV technique. First, the sensor's selectivity was performed in PB (pH 7.0) consisting of 200 μM FLU with the co-existence of a 50-fold excess concentration of possible interfering molecules such as 2-nitro aniline (2-NA), 2-nitro phenol (2-NP), chloramphenicol (CLP), 4-nitro aniline (4-NA), 4-nitro phenol (4-NP), 4-nitro benzene (4-NB), nitrofurantoin (NFT), and nitrofurazone (NFZ).

The corresponding DPV responses are displayed in Fig. 6c, which depicts that even at the higher concentration of interferents, the FLU's reduction peak current intensity is not much varied, and also, there is no shift in reduction peak potential. However, the nitro group containing interferents (50-fold excess) could produce a minor interference (< 18%) in the peak current response of FLU (200 μM), which is presented as a bar diagram in Fig. 6d. The experimental results indicate that the Co$_3$O$_4$@NPC/GCE has a reasonable selectivity to detect FLU in the aqueous solution. The sensor's reproducibility was then tested with parallel DPV measurements by five individual Co$_3$O$_4$@NPC/GCE electrodes (Fig. S4a). Out of the findings, only 2.4% of the relative standard deviation

was observed for the experiment. In addition, the developed sensor was stable for detection of FLU for up to 4 weeks, and 95.8% of the reduction peak (R1) current was observed after 4 weeks, indicating good stability of the sensor. The sensor's repeatability was performed by 10 continuous DPV experiments for the detection of 100 μM FLU in PB (pH 7.0). The corresponding results are shown in Fig. S4b, confirming the excellent repeatability of the established sensor. The observed results of Co$_3$O$_4$@NPC/GCE indicate that the Co$_3$O$_4$@NPC nanocomposite can be an effective electrode material for the sensitive detection of FLU.

Real sample analysis

The real-time use of the fabricated sensor was tested in the actual samples. The human urine sample was collected (from a healthy volunteer), which was centrifuged (6000 rpm), and the supernatant solution was kept in cooling condition (4 °C) not longer than 24 h. Then, a known concentration of FLU was spiked and then subjected to the analysis. The spiked human urine sample was diluted with PB (pH 7.0) at a 1:100 ratio. The analysis was then performed under similar experimental conditions as in sections 2.4 and 3.5, using Co$_3$O$_4$@NPC/GCE, and the results are shown in Fig. S4c. The FLU concentration was measured using the standard

addition procedure, and the analytical results are tabulated in Table S2. From the analytical result, it can be seen that the developed sensor exhibit ~ 98% recovery in the spiked human urine sample, and from the triplicate ($n = 3$) repeating experiments, the relative standard deviation (RSD) was found to be 1.7%. The observed results indicate that the sensor can exhibit good recovery efficiency in spiked urine samples, thus validating real-time application aptness.

Supercapacitor studies

To study supercapacitor performance, CVs of bare Ni foam and Co_3O_4@NPC nanocomposite-modified Ni foam (Co_3O_4@NPC/Ni foam) electrodes were recorded (Fig. 7a) within the voltage range of 0 to 0.6 V at the scan rate of 25 mV s^{-1} in 1M KOH electrolyte. The Co_3O_4@NPC/Ni foam electrode exhibited a prominent redox peak current area than bare Ni foam. During the forward scan in CV, the cobalt(III) oxide is initially oxidized into cobalt oxy-hydroxide, and it is further oxidized to cobalt(IV) oxide. Upon the reverse scan, the cobalt(IV) oxide is reduced into cobalt(III) oxide. The observed redox peak indicates the changes in the different oxidation states of Co_3O_4. The phenomenon is that the charge storage mechanism in Co_3O_4@NPC/Ni foam is mainly due to faradic redox reactions, which can be shown by the following equations as stated in the literature [16, 33].

$$Co_3O_4 + OH^- + H_2O \longleftrightarrow 3CoOOH + e^-$$
$$CoOOH + OH- \longleftrightarrow CoO_2 + H_2O + e^-$$
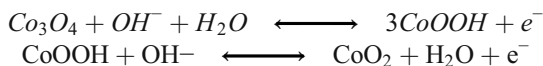
From the region of CVs, it can be shown that the specific capacitance was improved by the pseudocapacitance efficiency of the nanocomposite relative to bare Ni foam. This may be associated with the pseudo-capacitive involvement of the oxygen surface functional groups [34], which may improve wettability and increase the electroactive surface area [37]. Further, the different scan rate (5 to 50 mV s^{-1}) studies on Ni foam and Co_3O_4@NPC/Ni foam were also performed. When compared to the bare Ni foam (Fig. S5), the Co_3O_4@NPC/Ni foam exhibited a high redox peak response. As the scan rate is increased, the redox peak current increases, and the potential difference between the peaks is also increased (Fig. 7b) by the polarization of the electrode [2]. The observed result implies good electrochemical reversibility, and the redox peak currents are aligned with the scanning rate, which suggests that the overall process is surface controlled. To get further insight, Co_3O_4@NPC/Ni foam was examined by the GCD technique (Fig. 7c). The charge-discharge curve's appearance at current densities of 5.0, 4.0, 3.0, 2.0, and 1.5 A g^{-1} reflects the good coulombic efficiency of the electrode, and the calculated specific capacitances are 225, 250, 255, 350, and 525 F g^{-1} (Fig. 7d), respectively. A

decrease in specific capacitance at higher current densities is due to the phenomenon of Faradaic reaction resistance and ion diffusion resistance [3]. Further, the Co_3O_4@NPC/ Ni foam electrode's cycle durability at a current density of 3.0 A g^{-1} was achieved up to 8000 cycles (Fig. 7f) with 81% of capacitance retention. Notably, the electrode's specific capacitance decreased only up to 19% of its original capacitance value even after the 8000 cycles of charge-discharge, suggesting the material's excellent performance. It might be due to the combined performance rendered by the Co_3O_4 NPs and nitrogen-doped carbon matrix. Thus, the results indicate that the Co_3O_4@NPC electrode can have a good specific capacitance with strong cycle stability.

Electrochemical kinetics on the electrode/electrolyte interface was studied using the EIS experiment. The result is displayed in the form of a Nyquist plot, as shown in Fig. 7e. A well-marked semicircle was obtained for the higher frequency region and a vertical line for the lower frequency region, which is more consistent with the previous reports [34–36]. The semicircle diameter denotes the charge transfer resistance (R_{ct}) at the electrode/electrolyte interface.

Compared to bare Ni foam, the Co_3O_4@NPC/Ni foam electrode displayed a lower R_{ct} value and replicated the good electron transport at the electrode/electrolyte interface. Therefore, the analytical parameters indicated that Co_3O_4@NPC nanocomposite could be a hopeful electrode substrate for the application of a supercapacitor. Finally, the supercapacitor efficiency of Co_3O_4@NPC nanocomposite is comparable to certain state-of-the-art MOF materials derived from Co_3O_4 and summarized in Table S3. The distinction clearly indicates the significance of MOF-derived nanomaterials for the use of supercapacitors. The obtained capacitance of the Co_3O_4@NPC nanocomposite derived from ZIF-67 is comparable to most of the Co_3O_4 related materials published. The high performance may be due to the synergistic effect between the in situ–formed Co_3O_4 nanoparticles and the supporting carbon matrix, which significantly improves the electron transfer capability during electrochemical reactions. Moreover, the porous structure of the nanocomposite also enlarges the surface area with a greater number of active sites. Accordingly, the electrode surface wettability and the charge transfer at the electrode/electrolyte interface have been increased and caused stable electrochemical performances in both the detection of FLU and supercapacitor studies. Therefore, in this study, no major limitations have been observed, which makes the Co_3O_4@NPC nanocomposite a suitable electrode material for electrochemical applications.

Conclusion

In conclusion, the ZIF-67 was shown as an effective template for synthesizing cobalt oxide nanoparticles loaded with
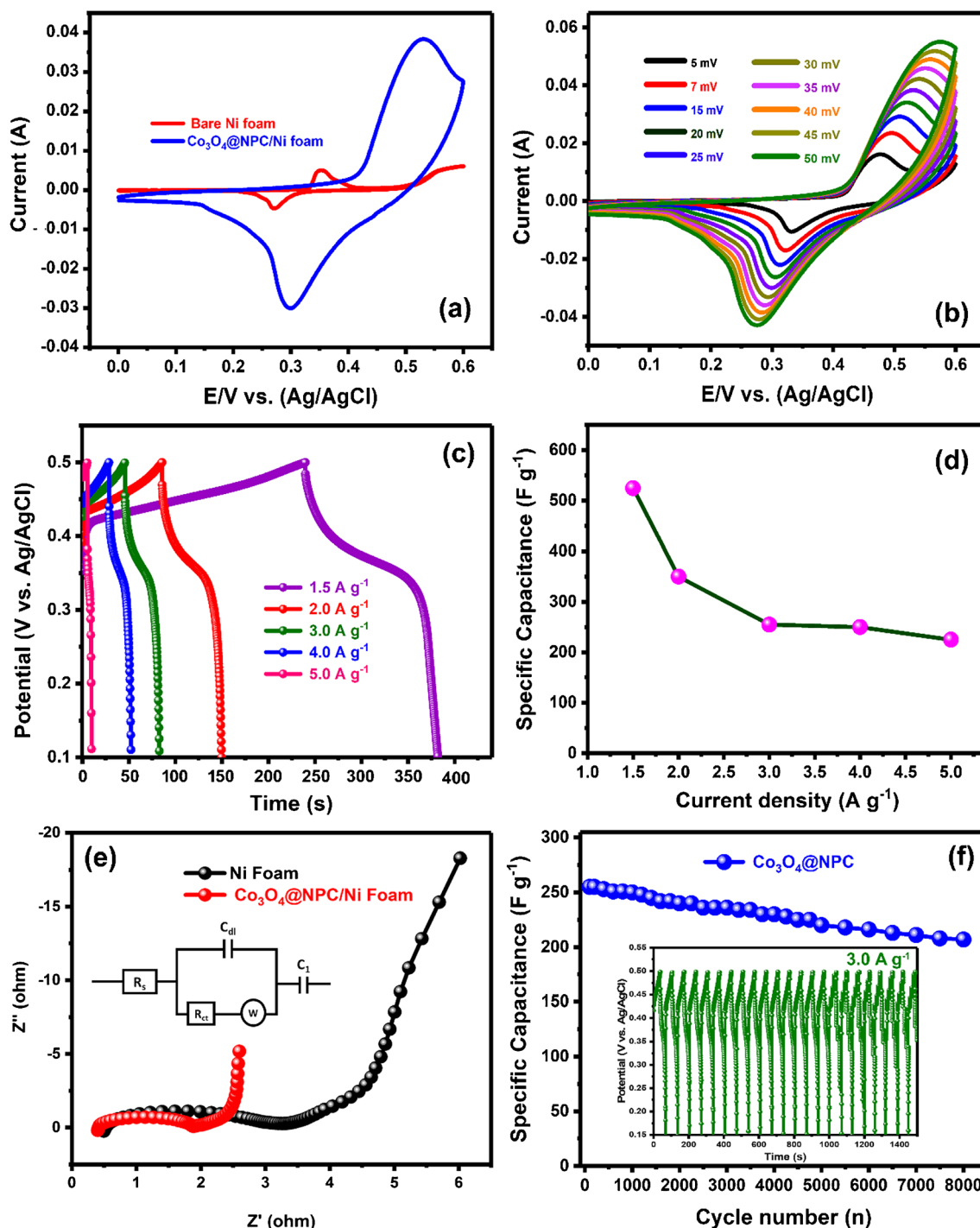
Fig. 7 The electrochemical activity of Co_3O_4@NPC-modified Ni foam electrode with 1.0 M KOH electrolyte. **a** Comparative CVs for the bare Ni foam and Co_3O_4@NPC electrodes at 25 mV s^{-1}, **b** CVs obtained from Co_3O_4@NPC electrode at varying scan rates, **c** galvanostatic charge-discharge curves of the Co_3O_4@NPC electrodes at current densities of 1.5, 2.0, 3.0, 4.0, and 5.0 A g^{-1}, **d** calibration plot between current density and specific capacitance, **e** EIS results of the electrodes, **f** cycle performance of the Co_3O_4@NPC electrode measured at the current density of 3.0 A g^{-1}

nitrogen-doped porous carbon (Co_3O_4@NPC) nanocomposite. The systematic characterization using various analytical techniques confirms nanocomposite's successful formation with nitrogen doping in the carbon matrix. Additionally, the in situ–formed cobalt oxide during the calcination process has

also catalyzed the carbon graphitization. The electrochemical sensor results strongly reveal that the catalytic behavior of Co_3O_4 and N-doped carbon matrix with a significant number of the active site and the porous structure of the nanocomposite are responsible for shortening the diffusion pathway to

detect the FLU with very low reduction potential (-0.42 V) than reported sensors. Moreover, the decent recovery performance of the sensor in the urine sample, suggesting its practical applicability. In addition to the sensor, the Co_3O_4@NPC-fabricated electrode outperforms much of the related state of the art by achieving significant specific capacitance (525 F g^{-1}) with reasonable cycling stability. Finally, the present study also paves the way for MOFs to be considered a suitable template for the one-step material synthesis with unique structure and their role in high-performance electrode material for electrochemical sensors and energy storage devices. However, in our opinion, the time variations in calcination of ZIF-67 may bring the different nanostructures to the nanocomposite and it may influence their electrochemical performances.

Declarations

Conflict of interest The authors declare that they have no competing interests.

References

1. Kadivar M, Aliakbar A (2021) A molecularly imprinted poly 2-aminophenol-gold nanoparticle-reduced graphene oxide composite for electrochemical determination of flutamide in environmental and biological samples. Anal Methods 13:536–551. https://doi.org/10.1039/d0ay01812k

2. Kesavan G, Chen SM (2021) Highly sensitive manganese oxide/hexagonal boron nitride nanocomposite: an efficient electrocatalyst for the detection of anti-cancer drug flutamide. Microchem J 163: 105906. https://doi.org/10.1016/j.microc.2020.105906

3. Rezaeifar Z, Rounaghi GH, Es'haghi Z, Chamsaz M (2018) Electrochemical determination of anticancer drug, flutamide in human plasma sample using a microfabricated sensor based on hyperbranchedpolyglycerol modified graphene oxide reinforced hollow fiber-pencil graphite electrode. Mater Sci Eng C 91:10–18. https://doi.org/10.1016/j.msec.2018.05.017

4. Hu X, Shi W, Wei S et al (2013) Occurrence and potential causes of androgenic activities in source and drinking water in China. Environ Sci Technol 47:10591–10600. https://doi.org/10.1021/es401464p

5. He H, Morely JE, Silva-Lopez E et al (2009) Synthesis and characterization of nonsteroidal-linked M(CO) 3+(M = 99mTc, Re) compounds based on the androgen receptor targeting molecule flutamide. Bioconjug Chem 20:78–86. https://doi.org/10.1021/bc8003183

6. Suresh PS, Srinivas NR, Mullangi R (2018) Review of HPLC and LC-MS/MS assays for the determination of various nonsteroidal anti-androgens used in the treatment of prostate cancer. Biomed Chromatogr 32:e4034. https://doi.org/10.1002/bmc.4034

7. Khan N, Abdelhamid HN, Yan JY et al (2015) Detection of flutamide in pharmaceutical dosage using higher electrospray ionization mass spectrometry (ESI-MS) tandem mass coupled with Soxhlet apparatus. Anal Chem Res 3:89–97. https://doi.org/10.1016/j.ancr.2015.01.001

8. Nagaraja P, Sunitha KR, Silwadi MF (2000) New spectrophotometric method for the determination of flutamide in pharmaceutical preparations. J Pharm Biomed Anal 23:617–622. https://doi.org/10.1016/S0731-7085(00)00319-8

9. Asif M, Liu H, Aziz A et al (2017) Core-shell iron oxide-layered double hydroxide: high electrochemical sensing performance of H2O2 biomarker in live cancer cells with plasma therapeutics. Biosens Bioelectron 97:352–359. https://doi.org/10.1016/j.bios.2017.05.057

10. Ashraf G, Asif M, Aziz A et al (2021) Rice-spikelet-like copper oxide decorated with platinum stranded in the CNT network for electrochemical in vitro detection of serotonin. ACS Appl Mater Interfaces 13:6023–6033. https://doi.org/10.1021/acsami.0c20645

11. Ramadhass KD, Ganesan M, Chen T-W et al (2021) 3D honeycomb like nitrogen self-doped porous carbon networks for high-performance electrochemical detection of antibiotic drug furazolidone. J Electrochem Soc 168:047503. https://doi.org/10.1149/1945-7111/abf21d

12. Muthusankar G, Sethupathi M, Chen SM et al (2019) N-doped carbon quantum dots @ hexagonal porous copper oxide decorated multiwall carbon nanotubes: a hybrid composite material for an efficient ultra-sensitive determination of caffeic acid. Compos Part B Eng 174:106973. https://doi.org/10.1016/j.compositesb.2019.106973

13. Muthusankar G, Sangili A, Chen SM et al (2018) In situ assembly of sulfur-doped carbon quantum dots surrounded iron(III) oxide nanocomposite; a novel electrocatalyst for highly sensitive detection of antipsychotic drug olanzapine. J Mol Liq 268:471–480. https://doi.org/10.1016/j.molliq.2018.07.059

14. Meng F, Fang Z, Li Z et al (2013) Porous Co3O4 materials prepared by solid-state thermolysis of a novel co-MOF crystal and their superior energy storage performances for supercapacitors. J Mater Chem A 1:7235–7241. https://doi.org/10.1039/c3ta11054k

15. Guo Y, Tang J, Salunkhe RR et al (2017) Effect of various carbonization temperatures on ZIF-67 derived Nanoporous carbons. Bull Chem Soc Jpn 90:939–942. https://doi.org/10.1246/bcsj.20170138

16. Saraf M, Rajak R, Mobin SM (2019) MOF derived high surface area enabled porous co $_3$ O $_4$ nanoparticles for supercapacitors. ChemistrySelect 4:8142–8149. https://doi.org/10.1002/slct.201901652

17. Wang Q, Astruc D (2020) State of the art and prospects in metal-organic framework (MOF)-based and MOF-derived nanocatalysis. Chem Rev 120:1438–1511

18. Wang H, Shao Y, Mei S et al (2020) Polymer-derived heteroatom-doped porous carbon materials. Chem Rev 120:9363–9419

19. Tahir MU, Arshad H, Xie W et al (2020) Synthesis of morphology controlled NiCo-LDH microflowers derived from ZIF-67 using binary additives and their excellent asymmetric supercapacitor properties. Appl Surf Sci 529:147073. https://doi.org/10.1016/j.apsusc.2020.147073

20. Lü Y, Zhan W, He Y et al (2014) MOF-templated synthesis of porous Co3O4 concave nanocubes with high specific surface area and their gas sensing properties. ACS Appl Mater Interfaces 6: 4186–4195. https://doi.org/10.1021/am405858v

21. Torad NL, Salunkhe RR, Li Y et al (2014) Electric double-layer capacitors based on highly graphitized nanoporous carbons derived from ZIF-67. Chem - A Eur J 20:7895–7900. https://doi.org/10.1002/chem.201400089

22. Torad NL, Kim J, Kim M et al (2020) Nanoarchitectured Porous Carbons Derived from ZIFs toward Highly Sensitive and Selective QCM Sensor for Hazardous Aromatic Vapors. J Hazard Mater 405: 124248. https://doi.org/10.1016/j.jhazmat.2020.124248

23. Zhou K, Mousavi B, Luo Z et al (2017) Characterization and properties of Zn/Co zeolitic imidazolate frameworks vs. ZIF-8 and ZIF-67. J Mater Chem A 5:952–957. https://doi.org/10.1039/C6TA07860E

24. Sheng P, Wang G, Dong M et al (2017) Systematic study of the crystallization process of CrAPO-5 using: in situ high resolution X-ray diffraction. RSC Adv 7:22964–22973. https://doi.org/10.1039/c6ra28572d

25. Zhang L, Zhao X, Ma W et al (2013) Novel three-dimensional Co_3O_4 dendritic superstructures: hydrothermal synthesis, formation mechanism and magnetic properties. CrystEngComm 15: 1389–1396. https://doi.org/10.1039/c2ce26374b

26. Ferrari AC, Basko DM (2013) Raman spectroscopy as a versatile tool for studying the properties of graphene. Nat Nanotechnol 8: 235–246. https://doi.org/10.1038/nnano.2013.46

27. Wang J, Tu J, Lei H, Zhu H (2019) The effect of graphitization degree of carbonaceous material on the electrochemical performance for aluminum-ion batteries. RSC Adv 9:38990–38997. https://doi.org/10.1039/C9RA07234A

28. Wei T, Zhang Q, Wei X et al (2016) A facile and low-cost route to heteroatom doped porous carbon derived from Broussonetia Papyrifera bark with excellent supercapacitance and CO2 capture performance. Sci Rep 6:1–9. https://doi.org/10.1038/srep22646

29. Madhu R, Veeramani V, Chen S-M et al (2015) Honeycomb-like porous carbon–cobalt oxide nanocomposite for high-performance enzymeless glucose sensor and supercapacitor applications. ACS Appl Mater Interfaces 7:15812–15820. https://doi.org/10.1021/acsami.5b04132

30. Ensafi AA, Talkhooncheh BM, Zandi-Atashbar N, Rezaei B (2020) Electrochemical sensing of flutamide contained in plasma and urine matrices using $NiFe_2O_4$/rGO nanocomposite, as an efficient and selective electrocatalyst. Electroanalysis 32:1717–1724. https://doi.org/10.1002/elan.202000048

31. Kubendhiran S, Sakthivel R, Chen S-M et al (2018) Innovative strategy based on a novel carbon-black−β-cyclodextrin nanocomposite for the simultaneous determination of the anticancer drug flutamide and the environmental pollutant 4-Nitrophenol. Anal Chem 90:6283–6291. https://doi.org/10.1021/acs.analchem.8b00989

32. Suvina V, Kokulnathan T, Wang T-J, Balakrishna RG (2020) Unraveling the electrochemical properties of lanthanum cobaltite decorated halloysite nanotube nanocomposite: an advanced electrocatalyst for determination of flutamide in environmental samples. Ecotoxicol Environ Saf 190:110098. https://doi.org/10.1016/j.ecoenv.2019.110098

33. Wang K, Yi X, Luo X et al (2016) Fabrication of Co_3O_4 pseudocapacitor electrodes from nanoscale cobalt–organic frameworks. Polyhedron 109:26–32. https://doi.org/10.1016/j.poly.2016.01.046

34. Luan VH, Han JH, Kang HW, Lee W (2019) Highly porous and capacitive copper oxide nanowire/graphene hybrid carbon nanostructure for high-performance supercapacitor electrodes. Compos Part B Eng 178:107464. https://doi.org/10.1016/j.compositesb.2019.107464

35. Xu C, Chen Y, Ma Y, et al (2020) Waste activated carbon transformed to electrode of supercapacitor through combining with Co(OH)2. Electrochim Acta 137475. https://doi.org/10.1016/j.electacta.2020.137475

36. Hekmat F, Shahrokhian S, Hosseini H (2019) Direct growth of nickel-cobalt oxide nanosheet arrays on carbon nanotubes integrated with binder-free hydrothermal carbons for fabrication of high performance asymmetric supercapacitors. Compos Part B Eng 172:41–53. https://doi.org/10.1016/j.compositesb.2019.05.027